Journal of Materials Chemistry A

ROYAL SOCIETY OF CHEMISTRY

PAPER

View Article Online
View Journal | View Issue

Cite this: *J. Mater. Chem. A*, 2023, **11**, 2225

Ultrathin metal–organic layers/carbon nitride nanosheet composites as 2D/2D heterojunctions for efficient CO_2 photoreduction†

Wei Yang,‡[ab] Xiao Lin,‡[a] Wen-Jie Shi,‡[a] Ji-Hong Zhang,[a] Yu-Chen Wang,[a] Ji-Hua Deng,*[a] Di-Chang Zhong*[a] and Tong-Bu Lu*[a]

Received 9th December 2022
Accepted 1st January 2023

DOI: 10.1039/d2ta09579c

rsc.li/materials-a

Metal–organic layers (MOLs), a new class of 2D photocatalysts with abundant readily accessible active sites, have emerged as a new 2D catalysis platform. Most pristine MOLs possess large band gaps and merely harvest ultraviolet light, which restricts their application in solar-driven CO_2 reduction. If MOLs are combined with visible-light-active semiconductors, it may overcome the shortage and construct efficient CO_2 reduction photocatalysts. Herein, a series of 2D/2D TM-MOLs/CN (TM = transition metal; CN = g-C_3N_4) heterogeneous composites were assembled by an *in situ* ultrasonic-assisted synthesis method. The resultant Co-MOL/CN(400) exhibited excellent photocatalytic CO_2 reduction performance, with a CO formation rate of 539 μmol h^{-1} g^{-1} and a selectivity of 79.8%. The proximity of the interfacial contact between Co-MOL and CN facilitates charge carrier separation/transfer from the photosensitizer to catalytic centers, which affords a superior photoactivity performance compared to most MOFs/CN (MOF = metal–organic frameworks) analogous hybrid photocatalysts. This heterogeneous composite thus represents a remarkable stepping stone in 2D/2D assembled multifunctional materials for studying the artificial photocatalytic reduction of CO_2 to solar chemicals and fuels.

1 Introduction

Sunlight-driven CO_2 conversion to fuels or chemicals is one of the most potent approaches to ease energy shortage and environmental crisis.[1–6] Porous metal–organic frameworks (MOFs) have provided a promising platform for photocatalytic CO_2 reduction due to their structural regularity and molecular tunability.[7–9] Pristine MOFs have exhibited good CO_2 photoreduction activity, such as Co-ZIF-9,[10] MIL-101(Fe),[11] NH_2-UiO-66 (Zr),[12] PCN-222,[13] and MAF-X27l-OH.[14] However, the insufficient active sites and poor mass/charge transfer ability of MOFs hinder their further activity enhancement in photocatalytic CO_2 reduction.

Shaping MOFs into 2-dimensional (2D) metal–organic layers (MOLs) has become a popular method to solve these obstacles. MOLs, as a new class of 2D crystalline catalysts, not only inherit the open double-sided planar structures and unique electronic properties of 2D materials but also overcome the mass/charge diffusion limitation. In addition, these exposed active sites in MOLs will more easily contact CO_2 molecules and speed up the reaction.[15–19] For instance, Lin *et al.* introduced M(bpy)$(CO)_3$X (M = Re or Mn) moieties into linear mono-carboxylic bipyridine ligand functionalized Hf_{12}–Ru MOLs, and the resulting Re–Ru Hf_{12} MOLs achieved a total turnover number (TON) of 8613 in photocatalytic CO_2-to-CO conversion.[20] Peng *et al.* combined Ni_3HITP_2 and rGO to construct a 2D/2D film, and the NHPG-2 film was able to achieve a high CO evolution rate of 3.8×10^4 μmol h^{-1} $g_{film}{}^{-1}$.[21] We firstly reported enhanced catalytic activity by tuning the exposed crystal facets in 2D Ni-based MOLs. The MOL, exposing rich (100) crystal facets (Ni-MOL-100), shows a much higher photocatalytic CO_2-to-CO activity than the one exposing (010) crystal facets (Ni-MOL-010).[22] Evidently, MOLs thus present a novel and reachable platform for studying CO_2 photoreduction.

To expand the application of MOLs in solar-driven photocatalytic CO_2 reduction, MOLs' photo-response ability needs to be enlarged because most pristine MOLs possess a large band gap and merely harvest ultraviolet (UV) light.[23–25] Inspired by the above studies, compositing MOLs with a visible-light-active semiconductor is an effective means to extend the photoresponse of MOLs towards the visible region. Graphitic carbon nitride (CN) is a desired candidate semiconductor. CN possesses a suitable band gap (≈2.7 eV) to harvest visible light. Their negative conduction band (CB) with sufficient thermodynamic energy could effectively promote CO_2

[a]*Institute for New Energy Materials & Low Carbon Technologies, School of Material Science & Engineering, School of Chemistry & Chemical Engineering, Tianjin University of Technology, Tianjin 300384, China. E-mail: djhycu_2006@aliyun.com; dczhong@email.tjut.edu.cn; lutongbu@tjut.edu.cn*

[b]*Institute of Coal Chemistry, State Key Laboratory of Coal Conversion, Chinese Academy of Sciences, Taiyuan 030001, China*

† Electronic supplementary information (ESI) available. See DOI: https://doi.org/10.1039/d2ta09579c

‡ These authors contributed equally to this work.

photoreduction.[26–30] This made CN popular in the photocatalytic energy conversion research community.[31–36] Consequently, coupling 2D MOL architectures with CN to form 2D/2D heterojunctions can realize the development of expected CO_2 photoreduction catalysts.[37,38] In 2D/2D MOLs/CN heterojunctions, intimately contacted interfaces between different layers of materials can ensure fast and efficient photo-generated carrier transfer and separation. Moreover, the CN may stabilize the MOLs in CO_2 photoreduction by performing as a substrate and template.

To implement this scheme, we synthesized a series of 2D/2D TM-MOLs/CN heterostructure photocatalysts by using a facile ultrasonic-assisted synthesis method. Owing to the unsaturated coordination sites and opposite charges in MOLs and CN, it is easy for them to form a stable 2D/2D configuration. Introducing MOLs into the surface of CN will generate more active sites and promote $e^- - h^+$ separation during the CO_2-to-CO conversion. The CO_2 reduction performance tests exhibit a strong dependence on the nature of the transition metal, not only in the yield of CO but also in terms of the CO/H_2 molar ratio. Particularly, the as-synthesized Co-MOL/CN(400) exhibits excellent visible-light photocatalytic CO_2 reduction performance, with the CO production rate of 539 μmol h^{-1} g^{-1}, much higher than those of CN, Co-MOL, Co-MOF/CN, and other TM-MOLs/CN composites in the same reaction. To the best of our knowledge, Co-MOL/CN(400) represents one of the most active noble-metal-free CN-based photocatalysts for CO_2 reduction.[39–41] This work provided instructive guidance for the rational design of MOL-based 2D/2D composites for photocatalytic CO_2 reduction.

2 Experimental

2.1. Materials

All chemicals and materials were commercially obtained and used without further purification. Nafion solution (5 wt%) was purchased from Alfa Aesar. All solutions used in the electrochemical experiments were prepared with Millipore water (18.2 MΩ). The purity of both argon and CO_2 is 99.999%. The MOLs and CN were synthesized according to the modified literature methods.

2.2. Preparation

The synthesis methods of CN and 2D MOL hybrid nanosheets have been reported in the literature.[42,43]

2.2.1 Synthesis CN nanosheets. CN was prepared by using urea as a precursor. Urea was placed in a tube furnace and heated to a specified temperature with a heating rate of 5 °C min^{-1}. The furnace cooled down to room temperature after being kept at 550 °C for 2 h in air. The collected light-yellow powder was ready for structural characterization and catalytic performance evaluation.

2.2.2 Synthesis of 2D MOL. In a typical procedure, terephthalic acid (24.9 mg, 0.15 mmol) and $Co(NO_3)_2 \cdot H_2O$ (43.7 mg, 0.15 mmol) were dissolved in 7.2 mL DMF/H_2O/ethanol (16 : 1 : 1) mixed solvent under ultrasonication. After getting the transparent solution, TEA (0.16 mL) was quickly injected into the above solution. Then, the colloidal solution was continuously ultrasonicated for several hours (40 kHz) under airtight conditions. Finally, the resulting precipitate was collected *via* centrifugation and washed with H_2O three times. The final product was dried at 50 °C for 12 h in an oven.

2.2.3 Preparation of 2D/2D Co-MOL/CN nanocomposites. In a typical procedure, a certain amount of CN (100, 200, 300, 400, 500, 600, or 800 mg) and $Co(NO_3)_2 \cdot H_2O$ (43.7 mg, 0.15 mmol) was dispersed in 7.2 mL DMF/H_2O/ethanol (16 : 1 : 1) mixed solvent with ultrasonication for 1 h. Then, 0.15 mmol H_2BDC was dissolved in the mixed solution and stirred for 0.5 h. Afterward, TEA (0.16 mL) was quickly injected into the solution and ultrasonicated (40 kHz) the colloidal solution for several hours under airtight conditions. Depending on the different masses of CN in Co-MOL/CN, the derived samples were labelled as Co-MOL/CN(100), Co-MOL/CN(200), Co-MOL/CN(300), Co-MOL/CN(400), Co-MOL/CN(500), Co-MOL/CN(600), and Co-MOL/CN(800), respectively.

3 Results and discussion

3.1. Fabrication and characterization of TM-MOL/CN

TM-MOL/CN composites were obtained in solution by *in situ* nucleation and oriented growth methods (Fig. 1a). As shown in Fig. S1,† pristine CN with abundant N sites and defect vacancies exhibited a negative zeta potential of −28.8 mV in pure water solution (pH ∼ 6.8). The transition metal precursor (Fe^{2+}, Co^{2+}, Ni^{2+}, Cu^{2+}) could steadily adsorb on the surface of CN by electrostatic interaction. When the organic linker terephthalic acid is added, it connects with the absorbed metal cations, and thus the formed TM-MOL would tightly anchor on the CN surface through an impregnation-ultrasound process (Fig. 1a). In addition, the represented Co-MOL presented a positive zeta potential (∼20.7 mV) (Fig. S1†). The electrostatic attraction between Co-MOL and CN could further enhance the 2D/2D composite structure stabilization and charge transfer

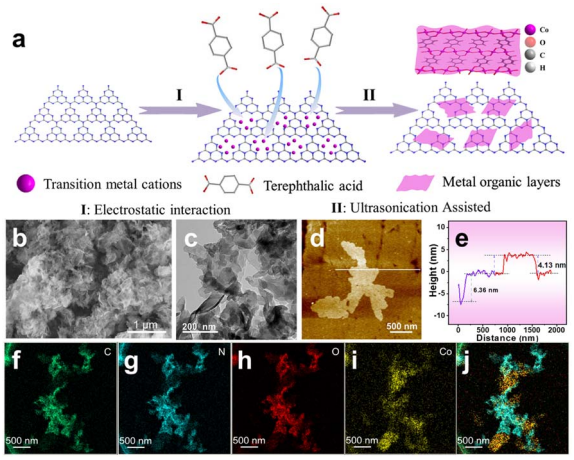

Fig. 1 (a) Schematic illustration of the synthesis procedure of MOLs onto the surface of CN. (b) HRSEM, (c) TEM, (d) AFM images, and (e) the corresponding height profiles of Co-MOL/CN(400). (f–j) EDX elemental mapping results of Co-MOL/CN(400).

efficiency. We obtained several Co-MOL/CN composites with different weight ratios of Co-MOL and CN, by varying CN amounts and named as Co-MOL/CN(x) (x = 100, 200, 300, 400, 500, 600, 800), respectively. The results of the Co content in Co-MOL/CN(x) composites were measured by inductively coupled plasma-mass spectroscopy and presented in Table S1.†

High resolution scanning electron microscope (HRSEM) and transmission electron microscopy (TEM) images show the CN surface is smooth with curled edges (Fig. S2a and S3a†), and Co-MOL presents a thin 2D layer structure (Fig. S2b and S3b†), while the Co-MOL/CN(400) surface displays grinding morphology (Fig. 1b). In the atomic force microscope (AFM) image (Fig. 1d and e), the thickness of Co-MOL/CNs is 10.5 ± 0.2 nm, corresponding to the height of CN (6.4 ± 0.6 nm) and Co-MOL (4.1 ± 0.3 nm) (Fig. S4†). Furthermore, TEM images of Co-MOL/CN(400) show that Co-MOL arrays (>100 nm) adsorbed on the CN surface tightly (Fig. 1c). The elemental mapping images of Co-MOL/CN(400) further evidence the successful growth of Co-MOL nanosheet arrays on the CN surface (Fig. 1f–j).

3.2. Structure characterization

The powder XRD of CN shows two diffraction peaks at 13.1° and 27.4° (Fig. 2a), which belong to the (100) and (002) planes (red line), respectively. The powder XRD of Co-MOL shows that the diffraction pattern is in good agreement with the simulation of $(Co_2(OH)_2(BDC)$; CCDC NO. 985792).[44] The diffraction peaks at 8.9°, 15.8°, and 17.8° correspond to the (200), (−201), and (400) crystal planes, respectively. As shown in Fig. 2a, the PXRD of the Co-MOL/CN composite shows diffraction peaks of two-phase (MOF and CN), further proving Co-MOF could grow on the rough CN surface. Along with the increase in the CN content, the intensities of diffraction peaks of Co-MOL become weaker. For different transition metal sample TM-MOL/CN composites, typical diffraction peaks of two-phase (MOL and CN) were also observed in the PXRD pattern (Fig. S5†). These results further illustrate the successful combination of TM-MOL and CN.

To further study the nature of the interactions between Co-MOL and CN, infrared spectra were screened for Co-MOL, CN, and Co-MOL/CN(400). The results show that for Co-MOL, there are two intense absorption bands at 1582 and 1355 cm^{-1}, which correspond to the characteristic peaks of ν_{as} ($-COO^-$) and ν_s ($-COO^-$) (Fig. S6†). The stretching vibration of OH, COO, and para-aromatic CH groups in pure Co-MOL are at ~3610 cm^{-1} and 3550–3000 cm^{-1}, respectively.[45] For CN, the typical stretching vibration bands presented at 1637, 1582, 1464, 1409, 1313, and 1245 cm^{-1} correspond to the characteristic peaks of heterocycles, and the peak at 816 cm^{-1} belongs to the triazine units.[46] Co-MOL/CN(400) contains the characteristic peaks of both Co-MOL and CN, despite the peak position and strength slightly changing. This result reveals the tight connection between Co-MOL and CN. UV-Vis absorption spectra show the light-harvesting capability of CN, Co-MOL, and Co-MOL/CN(400). As depicted in Fig. 2b, the pristine Co-MOL shows an ultraviolet-light absorption, which attributes to the π–π* transitions of organic ligands, and a visible-light adsorption (660 nm) that attributes to the d–d transition of Co^{2+} (d^7).[47] In contrast to Co-MOL and CN, the IR spectra of Co-MOL/CN(400) composites show visible absorption from 430 nm, similar to that of CN. The absorption edge of Co-MOL/CN(400) is also similar to that of CN, indicating that electron donor centres such as O were not doped into the crystal structure of CN.[48]

High-resolution X-ray photoelectron spectroscopy (XPS) further proves the strong interaction between Co-MOL and CN in Co-MOL/CN hybrid. The co-existing elements in Co-MOL/CN verify the successful immobilization of Co-MOL on the surface CN (Fig. S7†). The C 1s XPS spectra show two peaks at 284.8 and 288.5 eV (Fig. 3a), which can be assigned to the C–C or C=C and O=C–O species in Co-MOL.[49] In Fig. 3b, the peaks centred at 400.9, 399.9, and 398.6 eV correspond to the N–H, tertiary nitrogen N–$(C)_3$, and C–N=C groups in CN, respectively.[50,51] The binding energies of N 1s in the Co-MOL/CN hybrid shift to lower binding energies (Fig. 3b). On the contrary, the signals in Co-MOL appearing at 531.5 and 533.2 eV (corresponding to Co–O and C–O, respectively; Fig. 3c), positively shift after combining with CN. Considering the indiscernible alternation of the Co 2p peak shift (Fig. 3d), few Co ions were coordinated with CN. Therefore, according to the above observations, the strong interfacial connection between CN and Co-MOL may be derived from the CN···OH hydrogen bond.

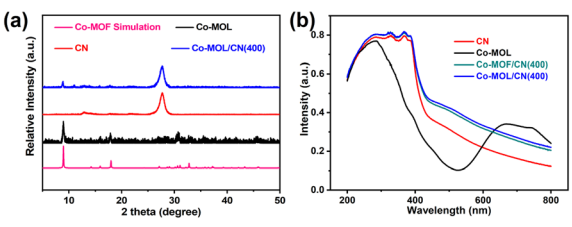

Fig. 2 (a) XRD patterns for different samples and XRD patterns of Co-MOL/CN composite with different CN contents and bare Co-MOL. (b) UV-Vis spectra of as-prepared Co-MOL, CN, Co-MOF/CN (400), Co-MOL/CN (400).

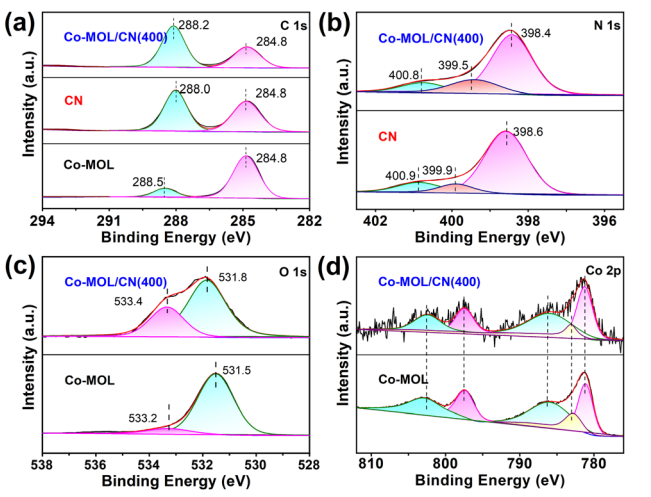

Fig. 3 High-resolution XPS spectra of (a) C 1s, (b) N 1s, (c) O 1s, and (d) Co 2p of CN, Co-MOL, and Co-MOL/CN(400).

3.3. Photocatalytic properties

The photocatalytic CO_2 reduction experiments by catalysts were investigated in a CH_3CN/H_2O/TEOA solution under visible light ($\lambda \geq 420$ nm) illumination. Typically, a 17 mL quartz vessel containing a mixture of 5 mL CO_2-saturated CH_3CN/H_2O/TEOA (v : v : v = 3 : 1 : 1) and catalysts (2 mg) was illuminated for a certain time. The gaseous products were detected by gas chromatography, and the liquid products were examined by ion chromatography. CO was the only carbon-based product of CO_2 reduction, and no other carbonaceous signals were detected.

In the control experiment, no noticeable CO was detected with Co-MOL, while with CN, the average CO production rate of 2.30 μmol g^{-1} h^{-1} was observed. After a small amount of Co-MOL combined with CN, the photocatalytic activity was enhanced remarkably. To optimize the selectivity and activity, we tuned the ratio of Co-MOL and CN. We found that the optimal catalyst was Co-MOL/CN(400), which produced 8.63 μmol CO and 2.17 μmol H_2 under 8 h irradiation (Fig. 4a), corresponding to the CO generated rate of 539.02 μmol $g^{-1}{}_{cat}$ h^{-1} and a CO selectivity of 79.80%. This CO_2 reduction rate is superior to many reported C_3N_4-based photocatalysts (Table S2†).

Along with the CN weight increasing from 0 to 400 mg, the amount of generated CO increases, but with a further increase in the CN weight, the amount of generated CO gradually decreases (Fig. 4b). This may be due to the excessive Co-MOL overlapping on the CN surface, impeding the light absorption of CN. The excessive Co-MOL may also act as a recombination centre for charge carriers during the photocatalytic reduction process. No appreciable CO or other hydrocarbon was detected without light irradiation, catalyst, or CO_2 introduction (Fig. 4c). $^{13}CO_2$ Isotopic experiment further confirmed the source of CO product. As shown in Fig. 4d, a peak with an m/z value of 29 corresponding to ^{13}CO appears, directly evidencing that the CO was generated from CO_2. In comparison, we also synthesized the bulky Co-MOF and prepared Co-MOF/CN(400) using a similar method (see ESI Fig. S8–9†). The photocatalytic activity of Co-MOF/CN(400) exhibits a lower CO yield (5.57 μmol; Fig. 4e), which indicates that the nanosheet array structure is beneficial to improve the photocatalytic performance of the MOF-CN composite. Physically mixed catalysts of Co^{2+}&CN, Co-MOF&CN, and Co-MOL&CN only produced 0.80, 1.59, and 2.78 μmol CO with a low CO selectivity of 27.35, 25.06, and 8.78% under the same conditions, respectively. These observations suggest that the close contact interface between Co-MOLs and CN is very important for activity enhancement.

We also prepared different transition-metal organic layers with CN by the same catalyst building method, including Ni-MOL/CN, Fe-MOL/CN, and Cu-MOL/CN (see ESI, Fig. S5†). The results of CO_2RR exhibit that the catalytic activity is strongly dependent on the nature of the transition metal. As displayed in Fig. S10,† only a certain amount of H_2 was detected for Fe-MOL/CN(400) and Cu-MOL/CN(400). Ni-MOL/CN(400) could produce CO in the reaction and the selectivity for CO was close to 100%; however, only 0.70 μmol CO was achieved in the photocatalytic system. These results demonstrate that Co-MOL/CN(400) is more efficient for photocatalytic reduction of CO_2 to CO than other tested TM-MOL/CN(400).

The photocatalytic recyclability of Co-MOL/CN(400) is examined with a 48 h photocatalytic reaction. As shown in Fig. 4f, it is observed that the activity of Co-MOL/CN(400) exhibits a negligible decrease in the sixth round of photocatalytic CO_2 reduction reaction, implying reliable stability of the composites. Furthermore, the robustness of Co-MOL/CN(400) was proved by PXRD and UV-vis spectra. The PXRD patterns and UV-vis spectroscopy of after-reaction Co-MOL/CN(400) show similar peaks to the freshly prepared Co-MOL/CN(400) (Fig. S11–12†). All those results support the good stability of Co-MOL/CN(400) during photocatalytic CO_2-to-CO conversion.

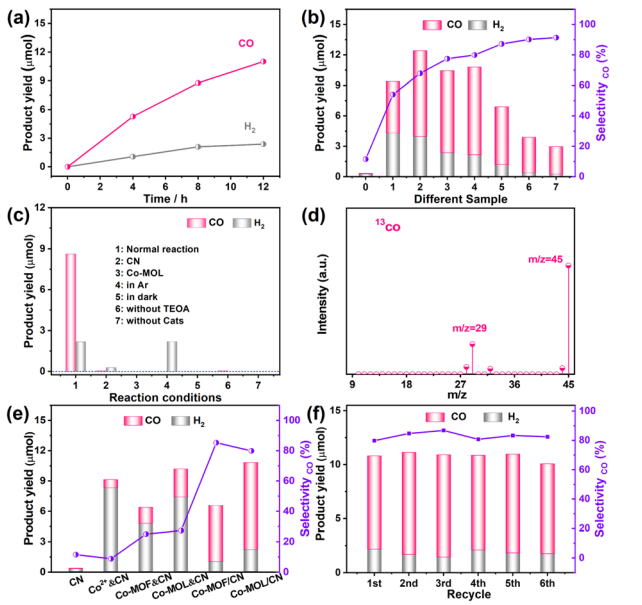

Fig. 4 (a) Time courses of photocatalytic CO_2 reduction for Co-MOL/CN(400). (b) CO production rates of CN and Co-MOL/CN(x) (0, 1, 2, 3, 4, 5, 6, and 7 correspond to CN, Co-MOL/CN(100), Co-MOL/CN(200), Co-MOL/CN(300), Co-MOL/CN(400), Co-MOL/CN(500), Co-MOL/CN(600), and Co-MOL/CN(800), respectively). (c) Control experiments of photocatalytic CO_2 reduction under different conditions. (d) Gas chromatography and mass spectroscopy analysis of the generated gas from the photocatalytic reduction of $^{13}CO_2$ by Co-MOL/CN(400). (e) CO_2 photoreduction performance over CN, Co^{2+}&CN(400), Co-MOF&CN(400), Co-MOL&CN(400), Co-MOF/CN(400), and Co-MOL/CN(400). (f) Durability tests for Co-MOL/CN(400).

3.4. Catalytic mechanism

Various complementary characterizations were performed to reveal the origin of the enhanced photocatalytic performance of Co-MOL/CN(400). As shown in Fig. 5a, the CO_2 adsorption isotherms of Co-MOL/CN(400) (3.07 cm^3 g^{-1}) and Co-MOF/CN(400) (2.64 cm^3 g^{-1}) exhibit better CO_2 adsorption performance than Co-MOL (1.69 cm^3 g^{-1}) and Co-MOF (0.81 cm^3 g^{-1}), which indicates that the introduction of CN is beneficial for increasing CO_2 adsorption. Relative to CN, the CO_2 adsorption of the composite materials slightly decreased. This may be

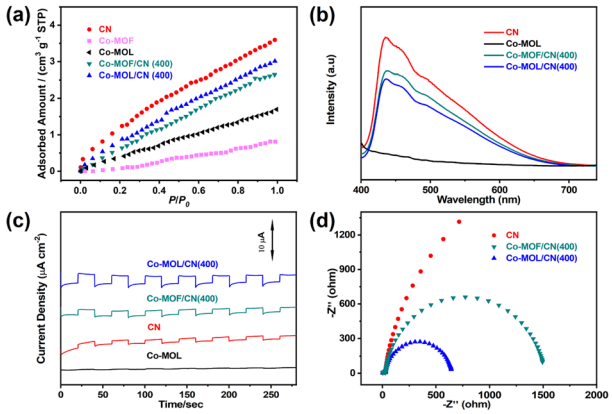

Fig. 5 (a) CO_2 adsorption isotherms and (b) PL spectra of CN, Co-MOF, Co-MOL, Co-MOF/CN(400), and Co-MOL/CN(400). (c) Transient photocurrent response of CN, Co-MOL, Co-MOF/CN(400) and Co-MOL/CN(400). (d) Nyquist plots of electrochemical impedance spectroscopy (EIS) of CN, Co-MOF/CN(400) and Co-MOL/CN(400) in 0.2 M Na_2SO_4 electrolyte.

attributed to the fact that Co-MOF or Co-MOL adhered to the CN surface, blocking the adsorption site of CO_2 in CN.[52] Furthermore, it is clearly found that Co-MOL/CN(400) shows a higher CO_2 adsorption capacity than Co-MOF/CN(400), further revealing that the exposure of more active sites facilitates the CO_2 adsorption capacity.

The steady-state photoluminescence (PL) emission measurements presented the separation efficiency of photogenerated charge carriers. In Fig. 5b, the CN sample exhibits a strong emission peak at ~436 nm under a 380 nm excitation. In comparison, the fluorescence peak intensity of Co-MOL/CN(400) decreases drastically, indicating the charge separation and transfer between CN and Co-MOF/CN(400) is efficient. Besides, the accelerated decay time-resolved photoluminescence (TRPL) and shortened charge-carrier averaged lifetimes ($\tau_{ave} = 1.83$ ns) for Co-MOL/CN(400) also illustrate the excellent electron transportability between Co-MOL to CN (Fig. S13, Table S3†).

To gain insight into the mechanism of the enhanced photocatalytic activity, we performed photocurrent curves and EIS plots curves to explore the photogenerated interface charge carrier separation and mobility efficiency. Compared with bare Co-MOL, CN, and Co-MOF/CN(400), the remarkably increased photocurrent density of Co-MOL/CN(400) confirmed the more efficient separation of the electron–hole pair due to 2D lamellar intimate interface between Co-MOLs and CN (Fig. 5c). Moreover, the EIS Nyquist plots of Co-MOL/CN composites exhibited significantly decreased semicircles than CN and Co-MOF/CN(400), indicating the faster charge transfer rate (Fig. 5d). Those results confirm that Co-MOL/CN(400) is the optimal catalyst for photochemical CO_2 reduction.

The ultrathin structure and large specific surface area of the Co-MOL/CN composites are greatly beneficial for exposing more active sites, expanding contact surface area, and promoting mass transport. In the Co-MOL/CN heterojunction, as Co-MOLs are uniformly loaded on the surface of CN sheets, constructing the heterojunction with excellent interfacial contact, interfacial charge transfer diffuse distances become shorter. In the pathway, the recombination of photoinduced electrons/hole pairs could be efficiently inhibited. The synergistic effect of the intimate contact from these heterojunctions between Co-MOL and CN can significantly enhance photocatalytic CO evolution performances.

To further clarify the electron transfer process in CO_2 reduction, we measured the bandgap and conduction band (CB) potentials of Co-MOL and CN. The bandgap energies of Co-MOL and CN are estimated to be 2.90 and 3.05 eV based on the Kubelka–Munk function, respectively (Fig. S14†). By Mott–Schottky plots (Fig. S15†), the positive slopes indicate that Co-MOL and CN have n-type semiconductor characteristics, and CB edge potentials of Co-MOL and CN are −1.12 and −1.24 V (*vs.* NHE), respectively (Fig. 6). Combined with their bandgaps, the valence band (VB) potentials of Co-MOL and CN are 1.93 and 1.66 V *vs.* NHE, respectively, as calculated by the equation: $E_{VB} = E_{CB} + E_g$. In this case, it is theoretically feasible for CN to transfer the electron to Co-MOL active sites because of the relative negative CB position of CN, thus accelerating the subsequent photocatalytic CO_2 reduction process under simulated sunlight irradiation. The holes in the VB of CN are quickly captured by the sacrificial reagents, which effectively separate photoexcited electrons and holes and then improve photocatalytic activity.

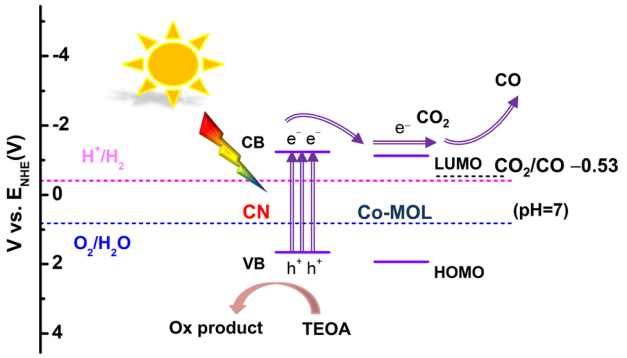

Fig. 6 Schematic illustration of charge transfer in Co-MOL/CN composites.

4 Conclusions

In conclusion, we have rationally assembled a series of transition-metal 2D MOLs with CN as CO_2 photoreduction catalysts. The 2D/2D ultrathin composites offered abundant active sites and high connected surface area, which remarkably hindered the photogenerated charge carrier recombination, and provided superior photocatalytic activity and selectivity for photocatalytic CO_2 reduction. As a result, the optimized Co-MOL/CN(400) shows a CO formation rate of 539 μmol h^{-1} g^{-1} with a selectivity of 79.8%. The efficient interfacial charge transfer between Co-MOL and CN is further confirmed by the steady-state PL spectra, transient photocurrent (TPC), and electrochemical impedance spectra (EIS). This study exhibited that 2D MOLs is an ideal platform and cocatalyst to advance

their performance tremendously. It offers an up-and-coming candidate to fabricate novel 2D MOF-based heterostructures for efficient photoreduction of CO_2 to value-added chemical feedstocks.

Author contributions

D. C. Z conceived and designed the project, W. Y, X. L, J. H. Z and Y. C. W performed the experiments, W. Y, W. J. S, J. H. D, D. C. Z and T. B. L analyzed the data and wrote the article.

Conflicts of interest

There are no conflicts to declare.

Acknowledgements

This work was supported by the National Key R&D Program of China (2022YFA1502902), the National Natural Science Foundation of China (22271218, 22071182, 22201209, 21931007), and China Postdoctoral Science Foundation (2022M713254).

References

1 H. Rao, L. C. Schmidt, J. Bonin and M. Robert, Visible-light-driven methane formation from CO_2 with a molecular iron catalyst, *Nature*, 2017, **548**, 74–77.
2 T. Ouyang, H.-J. Wang, H.-H. Huang, J.-W. Wang, S. Guo, W.-J. Liu, D.-C. Zhong and T.-B. Lu, Dinuclear metal synergistic catalysis boosts photochemical CO_2-to-CO conversion, *Angew. Chem., Int. Ed.*, 2018, **57**, 16480–16485.
3 J.-W. Wang, W.-J. Liu, D.-C. Zhong and T.-B. Lu, Nickel complexes as molecular catalysts for water splitting and CO_2 reduction, *Coord. Chem. Rev.*, 2019, **378**, 237–261.
4 T. Kong, J. Low and Y. Xiong, Catalyst: how material chemistry enables solar-driven CO_2 conversion, *Chem*, 2020, **6**, 1035–1038.
5 S.-L. Hou, J. Dong and B. Zhao, Formation of C−X bonds in CO_2 chemical fixation catalyzed by metal–organic frameworks, *Adv. Mater.*, 2020, **32**, 1806163.
6 S. Bai, H. Qiu, M. Song, G. He, F. Wang, Y. Liu and L. Guo, Porous fixed-bed photoreactor for boosting C–C coupling in photocatalytic CO_2 reduction, *eScience*, 2022, **2**, 428–437.
7 J. H. Zhang, Y. N. Gong, H. J. Wang, Y. C. Wang, W. Yang, J. H. Mei, D. C. Zhong and Lu Tong-Bu, Ordered heterogeneity of molecular photosensitizer towards enhanced photocatalysis, *Proc. Natl. Acad. Sci. USA*, 2022, **119**, e2118278119.
8 H. He, J. A. Perman, G. Zhu and S. Ma, Metal–organic frameworks for CO_2 chemical transformations, *Small*, 2016, **12**, 6309–6324.
9 J. W. Maina, C. Pozo-Gonzalo, L. Kong, J. Schütz, M. Hill and L. F. Dumée, Metal organic framework based catalysts for CO_2 conversion, *Mater. Horiz.*, 2017, **4**, 345–361.
10 S. Wang, W. Yao, J. Lin, Z. Ding and X. Wang, Cobalt imidazolate metal–organic frameworks photosplit CO_2 under mild reaction conditions, *Angew. Chem., Int. Ed.*, 2014, **53**, 1034–1038.
11 D. Wang, R. Huang, W. Liu, D. Sun and Z. Li, Fe-based MOFs for photocatalytic CO_2 reduction: role of coordination unsaturated sites and dual excitation pathways, *ACS Catal.*, 2014, **4**, 4254–4260.
12 D. Sun, Y. Fu, W. Liu, L. Ye, D. Wang, L. Yang, X. Fu and Z. Li, Studies on photocatalytic CO_2 reduction over NH_2-Uio-66(Zr) and its derivatives: towards a better understanding of photocatalysis on metal–organic frameworks, *Chem. Eur. J.*, 2013, **19**, 14279–14285.
13 H.-Q. Xu, J. Hu, D. Wang, Z. Li, Q. Zhang, Y. Luo, S.-H. Yu and H.-L. Jiang, Visible-light photoreduction of CO_2 in a metal–organic framework: boosting electron–hole separation *via* electron trap states, *J. Am. Chem. Soc.*, 2015, **137**, 13440–13443.
14 Y. Wang, N.-Y. Huang, J.-Q. Shen, P.-Q. Liao, X.-M. Chen and J.-P. Zhang, Hydroxide ligands cooperate with catalytic centers in metal–organic frameworks for efficient photocatalytic CO_2 reduction, *J. Am. Chem. Soc.*, 2018, **140**, 38–41.
15 X. Wang, P. She and Q. Zhang, Recent advances on electrochemical methods in fabricating two-dimensional organic-ligand-containing frameworks, *SmartMat*, 2021, **2**, 299–325.
16 A. Mukhopadhyay, V. K. Maka, G. Savitha and J. N. Moorthy, Photochromic 2D metal–organic framework nanosheets (MONs): design, synthesis, and functional MON-ormosil composite, *Chem*, 2018, **4**, 1059–1079.
17 L. Cao and C. Wang, Metal–organic layers for electrocatalysis and photocatalysis, *ACS Cent. Sci.*, 2020, **6**, 2149–2158.
18 G. Chakraborty, I.-H. Park, R. Medishetty and J. J. Vittal, Two-dimensional metal–organic framework materials: synthesis, structures, properties and applications, *Chem. Rev.*, 2021, **121**, 3751–3891.
19 J.-H. Dou, M. Q. Arguilla, Y. Luo, J. Li, W. Zhang, L. Sun, J. L. Mancuso, L. Yang, T. Chen, L. R. Parent, G. Skorupskii, N. J. Libretto, C. Sun, M. C. Yang, P. V. Dip, E. J. Brignole, J. T. Miller, J. Kong, C. H. Hendon, J. Sun and M. Dincă, Atomically precise single-crystal structures of electrically conducting 2D metal–organic frameworks, *Nat. Mater.*, 2021, **20**, 222–228.
20 G. Lan, Z. Li, S. S. Veroneau, Y.-Y. Zhu, Z. Xu, C. Wang and W. Lin, Photosensitizing metal–organic layers for efficient sunlight-driven carbon dioxide reduction, *J. Am. Chem. Soc.*, 2018, **140**, 12369–12373.
21 Q. Mu, W. Zhu, X. Li, C. Zhang, Y. Su, Y. Lian, P. Qi, Z. Deng, D. Zhang, S. Wang, X. Zhu and Y. Peng, Electrostatic charge transfer for boosting the photocatalytic CO_2 reduction on metal centers of 2D MOF/rGO heterostructure, *Appl. Catal. B*, 2020, **262**, 118144.
22 W. Yang, H.-J. Wang, R.-R. Liu, J.-W. Wang, C. Zhang, C. Li, D.-C. Zhong and T.-B. Lu, Tailoring crystal facets of metal–organic layers to enhance photocatalytic activity for CO_2 reduction, *Angew. Chem., Int. Ed.*, 2021, **60**, 409–414.
23 X. Hu, P. Chen, C. Zhang, Z. Wang and C. Wang, Energy transfer on a two-dimensional antenna enhances the

photocatalytic activity of CO_2 reduction by metal–organic layers, *Chem. Commun.*, 2019, **55**, 9657–9660.

24 B. Han, X. Ou, Z. Deng, Y. Song, C. Tian, H. Deng, Y.-J. Xu and Z. Lin, Nickel metal–organic framework monolayers for photoreduction of diluted CO_2: metal-node-dependent activity and selectivity, *Angew. Chem., Int. Ed.*, 2018, **57**, 16811–16815.

25 H.-L. Zheng, S.-L. Huang, M.-B. Luo, Q. Wei, E.-X. Chen, L. He and Q. Lin, Photochemical *in situ* exfoliation of metal–organic frameworks for enhanced visible-light-driven CO_2 reduction, *Angew. Chem., Int. Ed.*, 2020, **59**, 23588–23592.

26 Z. Han, Y. Yu, W. Zheng and Y. Cao, The band structure and photocatalytic mechanism for a CeO_2-modified C_3N_4 photocatalyst, *New J. Chem.*, 2017, **41**, 9724–9730.

27 Y. Li, X. Xu, J. Wang, W. Luo, Z. Zhang, X. Cheng, J. Wu, Y. Yang, G. Chen, S. Sun and L. Wang, Post-redox engineering electron configurations of atomic thick C_3N_4 nanosheets for enhanced photocatalytic hydrogen evolution, *Appl. Catal. B*, 2020, **270**, 118855.

28 R. Kuriki, K. Sekizawa, O. Ishitani and K. Maeda, Visible-light-driven CO_2 reduction with carbon nitride: enhancing the activity of ruthenium catalysts, *Angew. Chem., Int. Ed.*, 2015, **54**, 2406–2409.

29 M. Ou, W. Tu, S. Yin, W. Xing, S. Wu, H. Wang, S. Wan, Q. Zhong and R. Xu, Amino-assisted anchoring of $CsPbBr_3$ perovskite quantum dots on porous g-C_3N_4 for enhanced photocatalytic CO_2 reduction, *Angew. Chem., Int. Ed.*, 2018, **57**, 13570–13574.

30 X. Zhang, J. Yan, F. Zheng, J. Zhao and L. Y. S. Lee, Designing charge transfer route at the interface between WP nanoparticle and g-C_3N_4 for highly enhanced photocatalytic CO_2 reduction reaction, *Appl. Catal. B*, 2021, **286**, 119879.

31 K. Maeda, X. Wang, Y. Nishihara, D. Lu, M. Antonietti and K. Domen, Photocatalytic activities of graphitic carbon nitride powder for water reduction and oxidation under visible light, *J. Phys. Chem.*, 2009, **113**, 4940–4947.

32 J. Fu, J. Yu, C. Jiang and B. Cheng, g-C_3N_4-based heterostructured photocatalysts, *Adv. Energy Mater.*, 2018, **8**, 1701503.

33 Z. Jiang, X. Zhang, H.-S. Chen, X. Hu and P. Yang, Formation of g-C_3N_4 nanotubes towards superior photocatalysis performance, *ChemCatChem*, 2019, **11**, 4558–4567.

34 L. Yang, Y. Peng, X. Luo, Y. Dan, J. Ye, Y. Zhou and Z. Zou, Beyond C_3N_4 π-conjugated metal-free polymeric semiconductors for photocatalytic chemical transformations, *Chem. Soc. Rev.*, 2021, **50**, 2147–2172.

35 J. Liang, X. Yang, Y. Wang, P. He, H. Fu, Y. Zhao, Q. Zou and X. An, A review on g-C_3N_4 incorporated with organics for enhanced photocatalytic water splitting, *J. Mater. Chem. A*, 2021, **9**, 12898–12922.

36 Y. Lv, D. Ma, K. Song, S. Mao, Z. Liu, D. He, X. Zhao, T. Yao and J.-W. Shi, Graphitic carbon nitride decorated with C–N compounds broken by s-triazine unit as homojunction for photocatalytic H_2 evolution, *J. Mater. Chem. A*, 2023, **11**, 800–808.

37 C. Zheng, X. Qiu, J. Han, Y. Wu and S. Liu, Zero-dimensional-g-CNQD-coordinated two-dimensional porphyrin MOF hybrids for boosting photocatalytic CO_2 reduction, *ACS Appl. Mater. Interfaces*, 2019, **11**, 42243–42249.

38 L. Zhao, Z. Zhao, Y. Li, X. Chu, Z. Li, Y. Qu, L. Bai and L. Jing, The synthesis of interface-modulated ultrathin Ni(II) MOF/g-C_3N_4 heterojunctions as efficient photocatalysts for CO_2 reduction, *Nanoscale*, 2020, **12**, 10010–10018.

39 J.-H. Zhang, W. Yang, M. Zhang, H.-J. Wang, R. Si, D.-C. Zhong and T.-B. Lu, Metal-organic layers as a platform for developing single-atom catalysts for photochemical CO_2 reduction, *Nano Energy*, 2021, **80**, 105542.

40 G. Xu, H. Zhang, J. Wei, H.-X. Zhang, X. Wu, Y. Li, C. Li, J. Zhang and J. Ye, Integrating the g-C_3N_4 nanosheet with B–H bonding decorated metal–organic framework for CO_2 activation and photoreduction, *ACS Nano*, 2018, **12**, 5333–5340.

41 Y.-N. Gong, B.-Z. Shao, J.-H. Mei, W. Yang, D.-C. Zhong and T.-B. Lu, Facile synthesis of C_3N_4-supported metal catalysts for efficient CO_2 photoreduction, *Nano Res.*, 2022, **15**, 551.

42 S. Tang, X. Yin, G. Wang, X. Lu and T. Lu, Single titanium-oxide species implanted in 2D g-C_3N_4 matrix as a highly efficient visible-light CO_2 reduction photocatalyst, *Nano Res.*, 2019, **12**, 457–462.

43 C. Guo, Y. Jiao, Y. Zheng, J. Luo, K. Davey and S.-Z. Qiao, Intermediate modulation on noble metal hybridized to 2D metal–organic framework for accelerated water electrocatalysis, *Chem*, 2019, **5**, 2429–2441.

44 S. Zhao, Y. Wang, J. Dong, C.-T. He, H. Yin, P. An, K. Zhao, X. Zhang, C. Gao, L. Zhang, J. Lv, J. Wang, J. Zhang, A. M. Khattak, N. A. Khan, Z. Wei, J. Zhang, S. Liu, H. Zhao and Z. Tang, Ultrathin metal–organic framework nanosheets for electrocatalytic oxygen evolution, *Nat. Energy*, 2016, **1**, 16184.

45 A. Mesbah, P. Rabu, R. Sibille, S. Lebègue, T. Mazet, B. Malaman and M. François, From hydrated $Ni_3(OH)_2(C_8H_4O_4)_2(H_2O)_4$ to anhydrous $Ni_2(OH)_2(C_8H_4O_4)$: impact of structural transformations on magnetic properties, *Inorg. Chem.*, 2014, **53**, 872–881.

46 Q. Han, Z. Cheng, J. Gao, Y. Zhao, Z. Zhang, L. Dai and L. Qu, Mesh-on-mesh graphitic-C_3N_4@graphene for highly efficient hydrogen evolution, *Adv. Funct. Mater.*, 2017, **27**, 1606352.

47 A. Carton, A. Mesbah, T. Mazet, F. Porcher and M. François, Ab initio crystal structure of nickel(II) hydroxy-terephthalate by synchrotron powder diffraction and magnetic study, *Solid State Sci.*, 2007, **9**, 465–471.

48 X.-Q. Hao, Z.-W. Cui, J. Zhou, Y.-C. Wang, Y. Hu, Y. Wang and Z.-G. Zou, Architecture of high efficient zinc vacancy mediated Z-scheme photocatalyst from metal–organic frameworks, *Nano Energy*, 2018, **52**, 105–116.

49 J. Yang, P.-X. Xiong, C. Zheng, H.-Y. Qiu and M.-D. Wei, Metal−organic frameworks: a new promising class of materials for a high performance supercapacitor electrode, *J. Mater. Chem. A*, 2014, **2**, 16640–16644.

50 Z. Zhuang, Y. Li, Z. Li, F. Lv, Z. Lang, K. Zhao, L. Zhou, L. Moskaleva, S. Guo and L. Mai, MoB/g-C_3N_4 interface materials as a schottky catalyst to boost hydrogen evolution, *Angew. Chem., Int. Ed.*, 2018, **57**, 496–500.

51 A. Kumar, M. Khan, J. He and I. M. C. Lo, Visible-light-driven magnetically recyclable terephthalic acid functionalized g-C_3N_4/TiO_2 heterojunction nanophotocatalyst for enhanced degradation of PPCPs, *Appl. Catal.B*, 2020, **270**, 118898.

52 K.-Q. Lu, Y.-H. Li, F. Zhang, M.-Y. Qi, X. Chen, Z.-R. Tang, Y. M. A. Yamada, M. Anpo, M. Conte and Y.-J. Xu, Rationally designed transition metal hydroxide nanosheet arrays on graphene for artificial CO_2 reduction, *Nat. Commun.*, 2020, **11**, 5181.

